# Oxygen vacancy associated single-electron transfer for photofixation of $CO_2$ to long-chain chemicals

*Chen* et al.

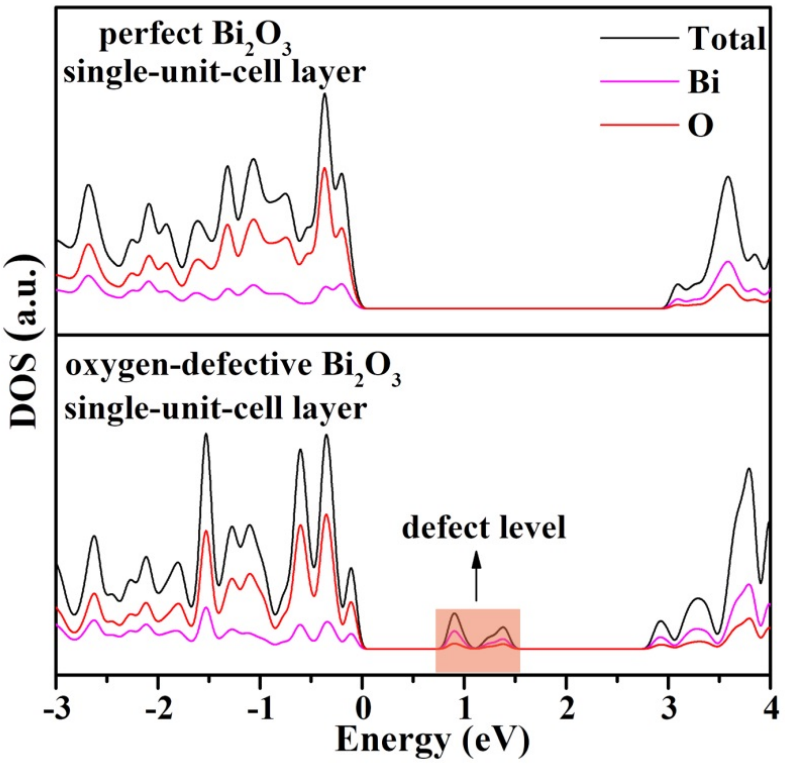


**Supplementary Figure 1.** Calculated density of states of perfect and oxygen-defective $Bi_2O_3$ single-unit-cell slab.

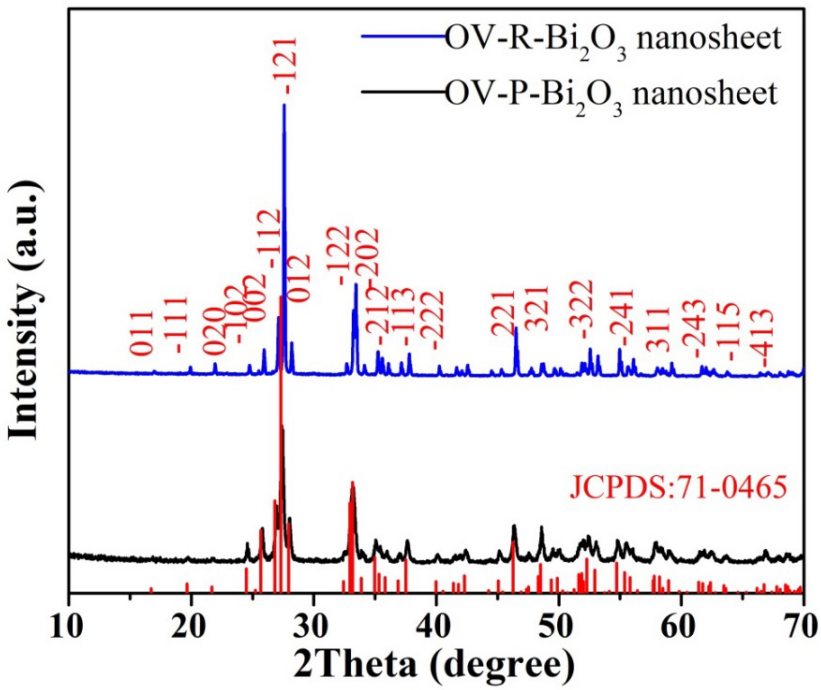


**Supplementary Figure 2.** XRD patterns of the $Bi_2O_3$ nanosheets with rich and poor oxygen vacancies.

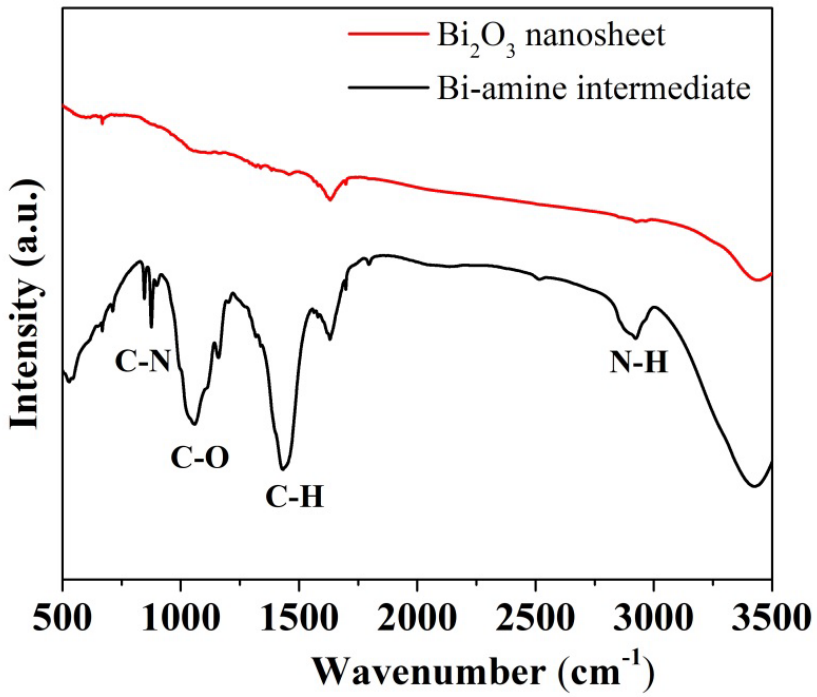


**Supplementary Figure 3.** IR spectra of Bi-amine hybrid intermediate and $Bi_2O_3$ nanosheets. The vibration bands suggest the existence of amine in Bi-amine hybrid intermediate. After ultrasonication and exfoliation, the vibration bands of amine are absent, indicating the clean surface of the as-prepared $Bi_2O_3$ nanosheets

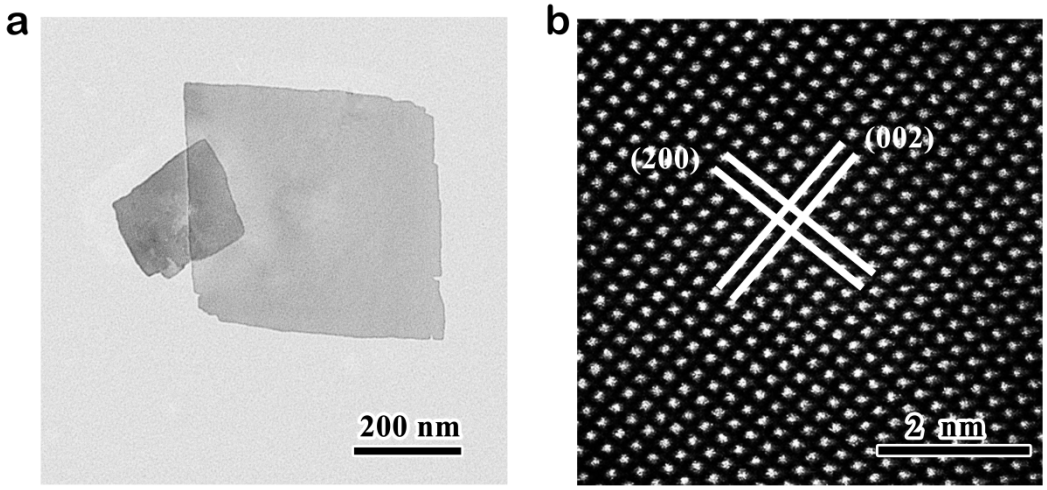


**Supplementary Figure 4.** (a) TEM image, and (b) atomic-resolution HAADF-STEM image of OV-P-$Bi_2O_3$ nanosheets.

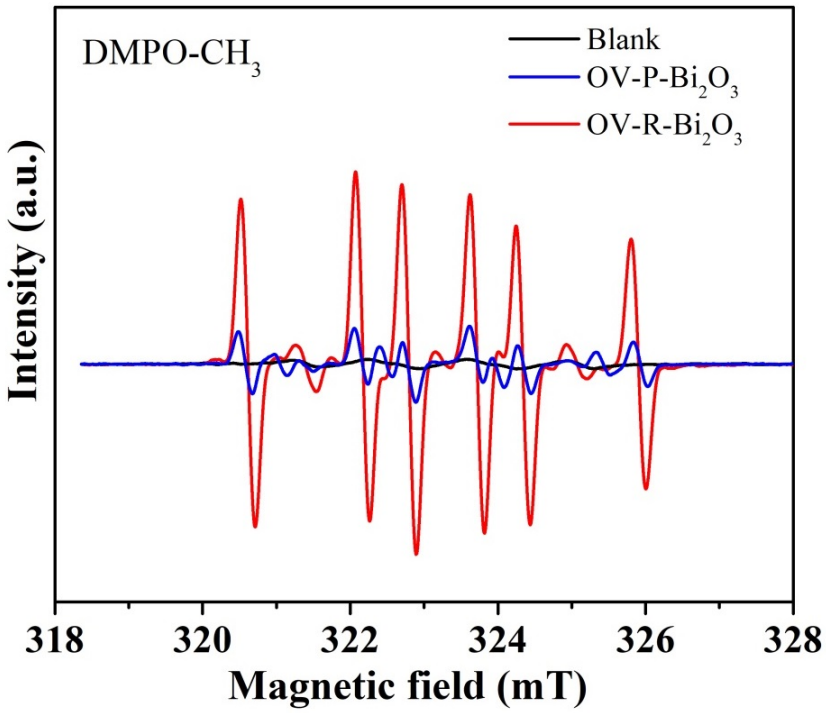


**Supplementary Figure 5.** *In-situ* ESR of DMPO-$CH_3$, where DMPO was used as the spin trapping agent.

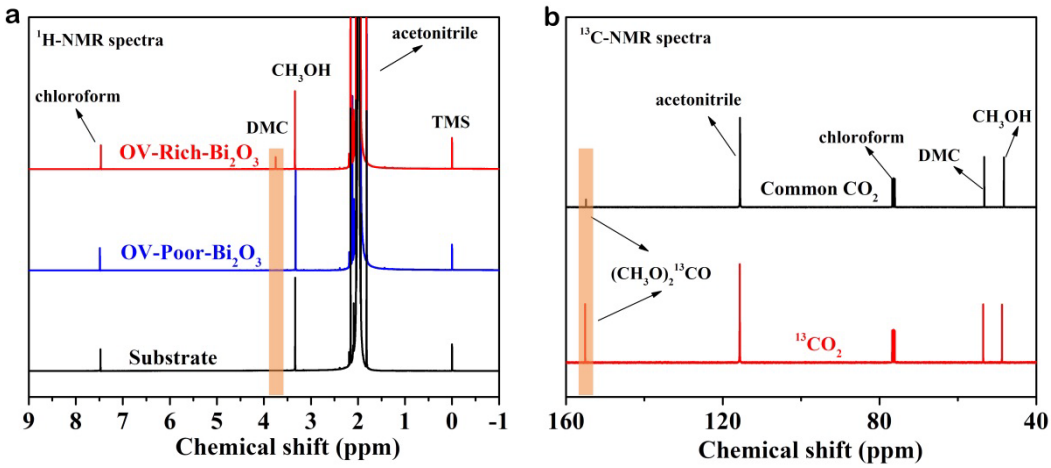


**Supplementary Figure 6.** Representative NMR spectra of synthetic DMC from the reaction of $CO_2$ and $CH_3OH$ in acetonitrile ($CH_3CN$) solution. (a) $^{1}$H-NMR spectra of the products after 8 h $CO_2$ reaction. (b) $^{13}$C-NMR spectra of the products using common $CO_2$ and $^{13}$C isotopic labeling $CO_2$.

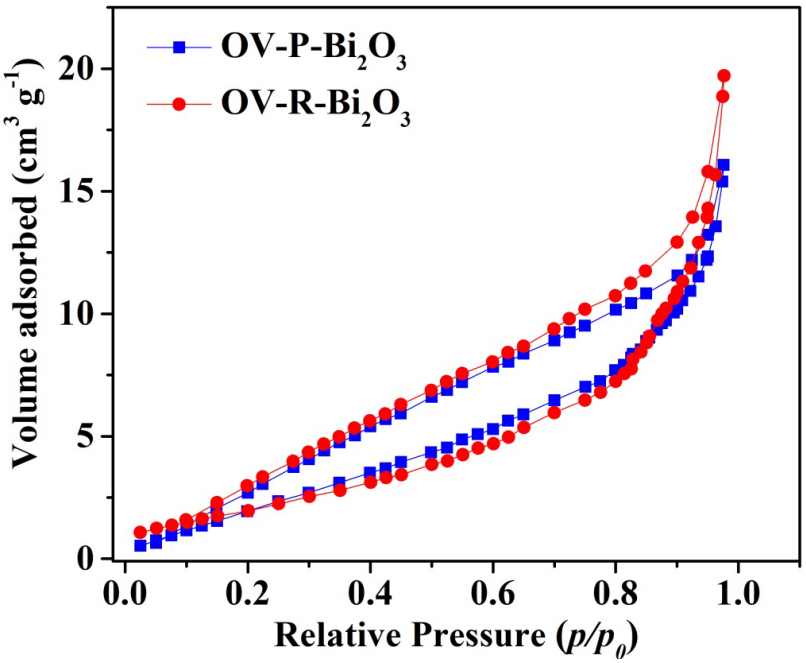


**Supplementary Figure 7.** BET surface area of OV-R-$Bi_2O_3$ and OV-P-$Bi_2O_3$ samples. The BET surface areas of OV-R-$Bi_2O_3$ and OV-P-$Bi_2O_3$ were 30.18 $m^2$ $g^{-1}$ and 28.96 $m^2$ $g^{-1}$, respectively, which suggests similar BET surface area of above samples.

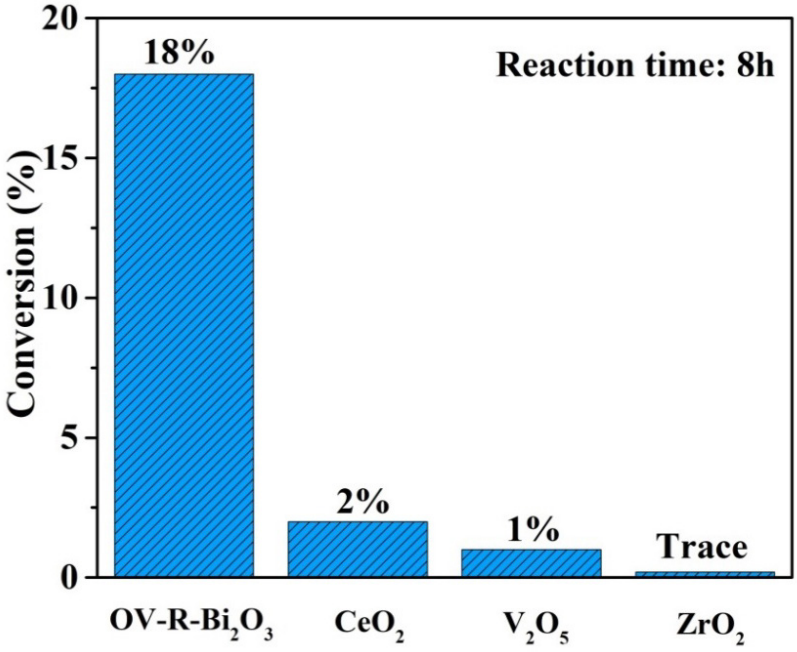


**Supplementary Figure 8.** Performances of various catalysts for $CO_2$ fixation to DMC under the same reaction conditions ($CO_2$ (0.2 Mpa) at 373 K under Xe-lamp irradiation). Herein, the $CeO_2$ nanosheets, $V_2O_5$ nanosheets, and $ZrO_2$ nanoparticles are prepared according to literatures[1-3].

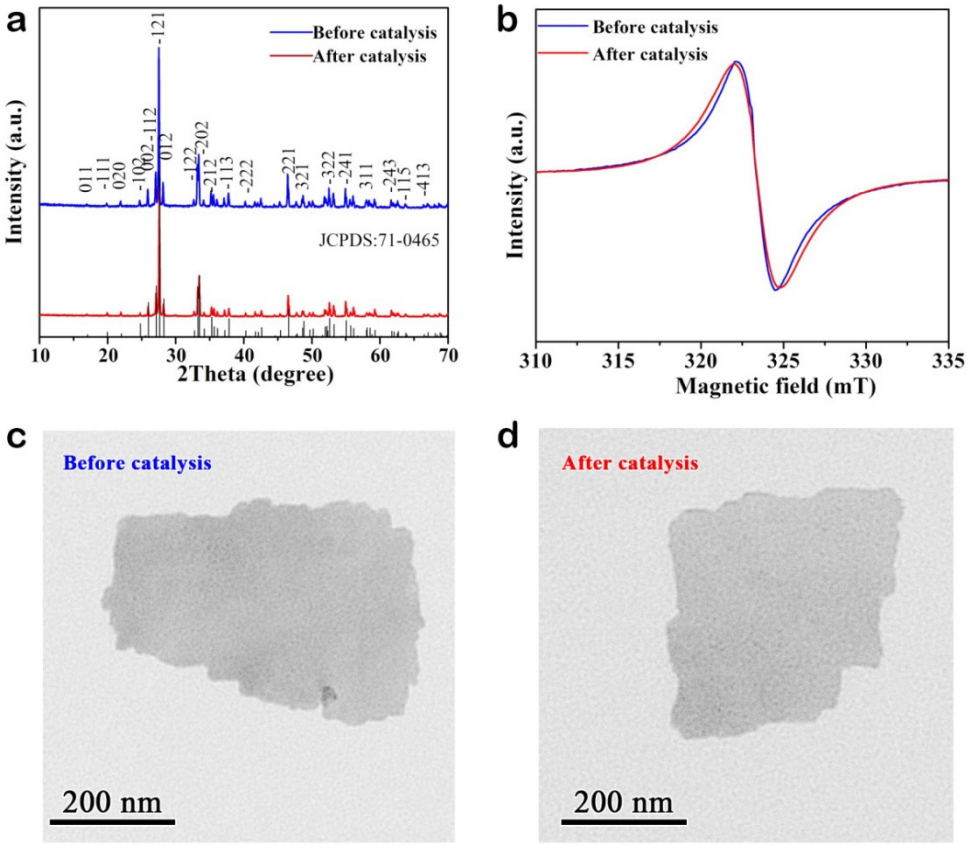


**Supplementary Figure 9.** Characterization of the OV-R-$Bi_2O_3$ sample after 25 catalytic cycles. (a) XRD pattern, (b) Room temperature ESR spectra, (c, d) TEM image before and after catalytic cycles up to 200 hours. The above results show that the crystal phase, morphology and vacancy concentration of OV-R-$Bi_2O_3$ were well maintained after 25 catalytic cycles.

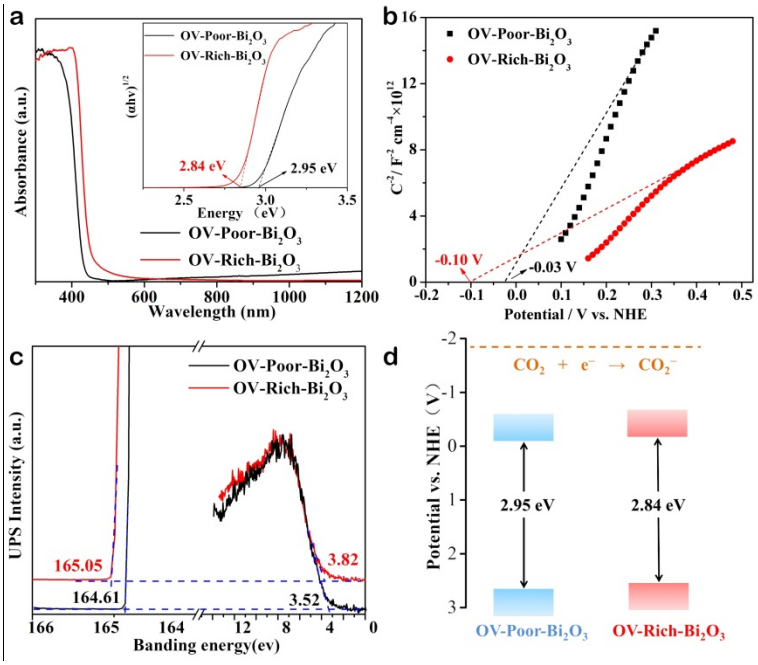


**Supplementary Figure 10.** Band structure study. (a) UV-vis spectra. Inset: corresponding Tauc plots of samples. (b) Mott-Schottky curves. (c) Valence-band spectra and Secondary electron cutoff ($E_{cut-off}$) measured by SRPES. (d) Band structure diagram. Based on the Mott-Schottky curves, the flat band potentials, which are close to the corresponding conduction band minima (CBMs) in n-type semiconductors, were determined to be −0.10 and −0.03 eV (vs. normal hydrogen electrode (NHE)) for OV-Rich-$Bi_2O_3$ and OV-Poor-$Bi_2O_3$ nanosheets, respectively. In addition, the valence band maxima (VBMs) of $Bi_2O_3$ nanosheets were resolved by synchrotron radiation photoelectron spectroscopy (SRPES) with excitation light ($hv$ = 168.4 eV)[4,5]. As demonstrated, the VBM of OV-Rich-$Bi_2O_3$ and OV-Poor-$Bi_2O_3$ nanosheets were estimated to be about −7.17 and −7.31 eV vs evac (vacuum level). With the combination of SRPES and UV–vis results, the CBMs of OV-Rich-$Bi_2O_3$ and OV-Poor-$Bi_2O_3$ nanosheets were estimated to be −0.11 and −0.08 eV (vs. NHE), in good agreement with the values estimated from Mott-Schottky curves. It is worth noting that the SRPES spectroscopy is more suitable for determining the band structures, as compared to the electrochemical method[6].

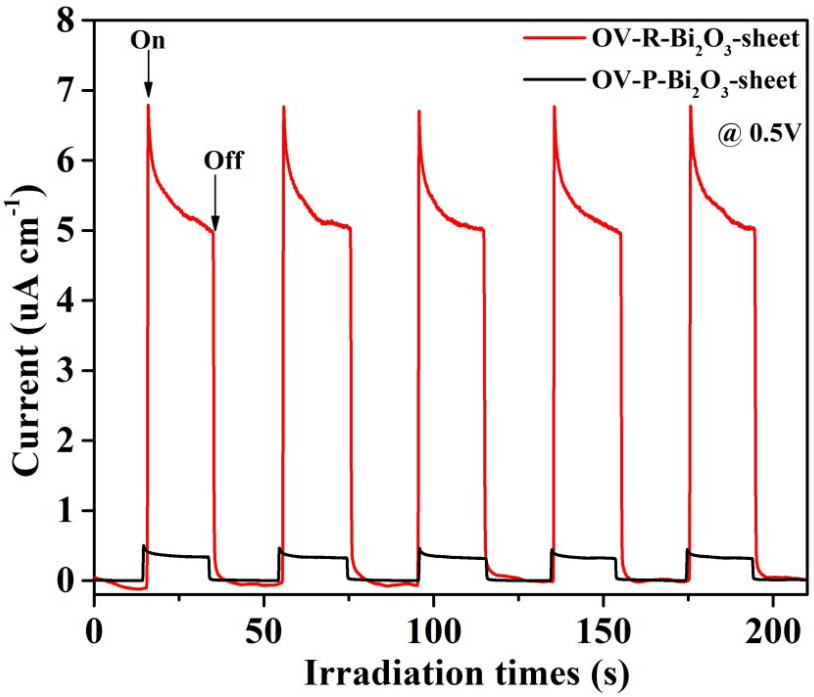


**Supplementary Figure 11**. Photocurrent response of $Bi_2O_3$ nanosheets with rich and poor oxygen vacancies, respectively. The photocurrent-voltage curves suggest enhanced photocurrent response under negative bias, confirming the enhanced photogeneration of hot electrons in the ultrathin $Bi_2O_3$-sheets with rich defects.

**Supplementary Table 1.** Direct synthesis of DMC from $CO_2$ and $CH_3OH$ with different catalysts.

| Catalyst | Conversion yield[a]（%） | Selectivity[b] (%) | Reaction condition | Ref. |
|---|---|---|---|---|
| **$Bi_2O_3$-bulk** | Trace | Trace | 0.2 Mpa, 373K,light, 8h | This work |
| **OV-P-$Bi_2O_3$ nanosheet** | 2 | >99 | 0.2 Mpa, 373K,light, 8h | This work |
| **OV-R-$Bi_2O_3$ nanosheet** | **18** | **>99** | 0.2 Mpa, 373K,light, 8h | This work |
| $ZrO_2$-KCl-$K_2CO_3$ | 10.8 | 43.2 | 9.5 Mpa, 423K, 8h | 7 |
| $Mg(OCH_3)_2$ + $ZrO_2$-KCl | 3.9 | 45.6 | 9.5 Mpa, 423K, 8h | 7 |
| $H_3PO_4/V_2O_5$ | 1.96 | 93.1 | 0.6 Mpa, 413K, 8h | 8 |
| $H_3PW_{12}O_{40}/ZrO_2$ | 2.02 | >99 | 7.6 Mpa, 373K, 7h | 9 |
| $CeO_2$- $ZrO_2$ | 0.8 | >99 | 6 Mpa, 383K, 24h | 10 |
| $Co_{1.5}PW_{12}O_{40}$ | 3.8 | 65.2 | 0.5 Mpa, 373K, 5h | 11 |
| Mo-Cu-Fe/$SiO_2$ | 7 | 88 | 0.5 Mpa, 393K, 4h | 12 |

[a]Determined by NMR analyses, using s-trioxane as the internal standard, mol %

[b]selectivity = $yield_{DMC}$*2/$conversion_{methanol}$

## Supplementary References


1 Sun, Y., Liu, Q., Gao, S., Cheng, H., Lei, F., Sun, Z., Jiang, Y., Su, H., Wei, S. & Xie, Y. Pits confined in ultrathin cerium(IV) oxide for studying catalytic centers in carbon monoxide oxidation. *Nature Commun.* **4**, 2899 (2013).

2 Peng, X., Zhang, X., Wang, L., Hu, L., Cheng, S. H.-S., Huang, C., Gao, B., Ma, F., Huo, K. & Chu, P. K. Hydrogenated $V_2O_5$Nanosheets for Superior Lithium Storage Properties. *Adv. Funct. Mater.* **26**, 784-791 (2016).

3 Fakhri, A., Behrouz, S., Tyagi, I., Agarwal, S. & Gupta, V. K. Synthesis and characterization of $ZrO_2$ and carbon-doped $ZrO_2$ nanoparticles for photocatalytic application. *J. Mol. Liq.* **216**, 342-346 (2016).

4 Zhang, N., Li, X., Ye, H., Chen, S., Ju, H., Liu, D., Lin, Y., Ye, W., Wang, C., Xu, Q., Zhu, J., Song, L., Jiang, J. & Xiong, Y. Oxide Defect Engineering Enables to Couple Solar Energy into Oxygen Activation. *J. Am. Chem. Soc.* **138**, 8928-8935 (2016).

5 Liu, W., Cao, L., Cheng, W., Cao, Y., Liu, X., Zhang, W., Mou, X., Jin, L., Zheng, X., Che, W., Liu, Q., Yao, T. & Wei, S. Single-Site Active Cobalt-Based Photocatalyst with a Long Carrier Lifetime for Spontaneous Overall Water Splitting. *Angew. Chem. Int. Ed.* **56**, 9312-9317 (2017).

6 Liu, J., Liu, Y., Liu, N., Han, Y., Zhang, X., Huang, H., Lifshitz, Y., Lee, S. T., Zhong, J. & Kang, Z. Water splitting. Metal-free efficient photocatalyst for stable visible water splitting via a two-electron pathway. *Science* **347**, 970-974 (2015).

7 Eta, V., Mäki-Arvela, P. i., Leino, A.-R., Kordás, K. n., Salmi, T., Murzin, D. Y. & Mikkola, J.-P. Synthesis of Dimethyl Carbonate from Methanol and Carbon Dioxide: Circumventing Thermodynamic Limitations. *Ind. Edg. Chem. Res.* **49**, 9609-9617 (2010).

8 Wu, X. L., Xiao, M., Meng, Y. Z. & Lu, Y. X. Direct synthesis of dimethyl carbonate on $H_3PO_4$ modified $V_2O_5$. *J. Mol. Catal. A: Chem.* **238**, 158-162 (2005).

9 Jiang, C., Guo, Y., Wang, C., Hu, C., Wu, Y. & Wang, E. Synthesis of dimethyl carbonate from methanol and carbon dioxide in the presence of polyoxometalates under mild conditions. *Appl. Catal., A* **256**, 203-212 (2003).

10 Tomishige, K. & Kunimori, K. Catalytic and direct synthesis of dimethyl

carbonate starting from carbon dioxide using $CeO_2$-$ZrO_2$ solid solution heterogeneous catalyst: effect of H2O removal from the reaction system. *Appl Catal a-Gen* **237**, 103-109 (2002).

11 Aouissi, A., Apblett, A. W., Al-Othman, Z. A. & Al-Amro, A. Direct synthesis of dimethyl carbonate from methanol and carbon dioxide using heteropolyoxometalates: the effects of cation and addenda atoms. *Transition Met. Chem.* **35**, 927-931 (2010).

12 Zhou, Y.-J., Xiao, M., Wang, S.-J., Han, D.-M., Lu, Y.-X. & Meng, Y.-Z. Effects of Mo promoters on the Cu–Fe bimetal catalysts for the DMC formation from $CO_2$ and methanol. *Chin. Chem. Lett.* **24**, 307-310 (2013).